

# Deformation mechanisms and damage in $\alpha$ -alumina under hypervelocity impact loading

Cheng Zhang,<sup>1</sup> Rajiv K. Kalia,<sup>1</sup> Aiichiro Nakano,<sup>1</sup> Priya Vashishta,<sup>1,a)</sup> and Paulo S. Brancio<sup>2</sup>

<sup>1</sup>*Collaboratory for Advanced Computing and Simulations, Department of Chemical Engineering and Materials Science, Department of Physics and Astronomy, and Department of Computer Science, University of Southern California, Los Angeles, California 90089-0242, USA*

<sup>2</sup>*Departamento de Física, Universidade Federal de São Carlos, São Carlos, São Paulo 13565, Brazil*

(Received 17 September 2007; accepted 8 January 2008; published online 17 April 2008)

Deformation mechanisms in  $\alpha$ -alumina under hypervelocity impact are investigated using molecular dynamics simulations containing  $540 \times 10^6$  atoms. A cylindrical projectile impacting normal to the (0001) surface at 18 km/s generates large temperature and pressure gradients around the impact face, and consequently local amorphization of the substrate in a surrounding hemispherical region is produced. Away from the impact face, a wide range of deformations emerge and disappear as a function of time under the influence of local stress fields, e.g., basal and pyramidal slips and basal and rhombohedral twins, all of which show good agreement with the experimental and theoretical results. New deformation modes are observed, such as twins along  $\{0\bar{1}11\}$ , which propagate at a roughly constant speed of 8 km/s and nucleate a large amount of defects where subsequent fractures initiate. The relation between deformation patterns and local stress levels is investigated. During unloading, we observe that microcracks nucleate extensively at the intersections of previous deformations within an hourglass-shaped volume that connects top and bottom free surfaces. From the simulation, the fracture toughness of alumina is estimated to be  $2.0 \pm 0.5$  MPa $\sqrt{\text{m}}$ . The substrate eventually fails along the surface of the hourglass region during spallation when clusters of substrate material are ejected from both free surfaces. © 2008 American Institute of Physics. [DOI: [10.1063/1.2891797](https://doi.org/10.1063/1.2891797)]

## I. INTRODUCTION

Necessitated by the research needs in defense and space programs, hypervelocity impact experiments have been carried out on a wide range of solids since the 1950s.<sup>1</sup> These materials include metals, ceramics, polymers, and other types of composites, whose response under shock compression is of major interest.<sup>2,3</sup> The studies help improve the armor performance in weapon systems<sup>4,5</sup> as well as the spacecraft shielding against meteoroid and orbital debris.<sup>6–8</sup> Ceramics are promising candidates for these applications because of their low density, high compressive strength, and high melting point to withstand low-velocity impact. In many weapon systems that require mobility, ceramic tiles have replaced the traditional metal armor. Similarly, ceramic coating is popular in aeronautical and aerospace industry. However, their brittleness, poor tensile and shear strength, and vulnerability to fracture limit their mechanical performance under hypervelocity impact. It is very important to understand the shock-induced microscopic processes and deformation mechanisms in ceramics, such as localized amorphization<sup>9</sup> and structural phase transformation.<sup>10</sup> Subhash and Ravichandran have performed experiments to study the loading response of an AlN crystal under high strain rates.<sup>11</sup> Shih *et al.* have identified through experiments sev-

eral deformation modes that lead to microcracks and eventual fracture in SiC.<sup>12</sup> Other extensively studied ceramics include Al<sub>2</sub>O<sub>3</sub> (alumina), B<sub>4</sub>C, and Si<sub>3</sub>N<sub>4</sub>.

Alumina is one of the most important structural ceramics due to its remarkable hardness, strong oxidation resistance, high melting temperature, and high compressive strength.<sup>13</sup> Compressive behavior of alumina, which is a constituent part of earth mantle, has been investigated by Karki *et al.*<sup>14</sup> Rosenberg *et al.*<sup>15</sup> have measured the dynamic compression strength of alumina subjected to plate impact. Mashimo *et al.*<sup>16</sup> have obtained its elastoplastic properties and Hugoniot diagrams. Grady<sup>17</sup> has measured its equation of state. The planar shock in these experiments is generated by gun-accelerated projectile plates, which can reach an impact velocity higher than 16 km/s (Ref. 18) with latest techniques. Observational techniques such as inclined mirrors and high-speed x-ray photography provide real-time measurements and imaging. Postshock samples are analyzed using high-resolution electron microscopy, transmission electron microscopy, or optical micrography to reveal damage morphology down to nanometer scale.

The fracture processes of alumina crystal under compressive loading have also been extensively studied.<sup>19–22</sup> Lankford *et al.* have discovered that microcracks form through the interaction of twinning or slip with grain boundary.<sup>19</sup> Similarly, Staehler *et al.* have identified crack initiation from dislocation pileup at grain boundaries.<sup>21</sup> For alumina single crystal, Chan and Lawn have carried out in-

<sup>a)</sup>Electronic mail: priyav@usc.edu.

dentation on sapphire and observed that microcracks nucleate from basal twin interfaces and pyramidal slip planes (SPs).<sup>20</sup> Meanwhile, unique transitions in fracture mechanisms have been reported by Sherman and Be'ery when cracks propagate in sapphire under bending.<sup>22</sup> However, the fracture mechanisms of ceramics are very sensitive to the strain rate of compressive loading.<sup>17,23</sup> Under low strain rates, ceramics have almost constant strengths as they fail at critical stresses when pre-existing defects (microcracks) coalesce. Their strengths are dramatically higher under ultrahigh strain rates as compressive shock wave propagates faster than cracks and suppresses fracture. On the other hand, high strain rate loading generates damages of much higher density than pre-existing defects, which facilitates failure in the unloading phase.

These results help understand the nature of shock response and fracture mechanisms in alumina. However, due to the limited spatiotemporal resolution of current experimental techniques, little is known about atomistic mechanisms of deformation and fracture process under hypervelocity impact (strain rate  $>10^4 \text{ s}^{-1}$ ), which is important for alumina shields against ballistic or meteoroidal impact. Computer simulations can help understand microscopic processes under such high strain rate loading.

As the available computing power has been increasing for the past few decades, people have been able to adopt more complex and accurate simulation representations, from the early one dimensional continuum model to later three dimensional (3D) wave propagation and hydrodynamic grid model.<sup>24</sup> These grid models can simulate materials under impact of life-size projectiles.<sup>25</sup> However, these models are incapable of reproducing atomistic deformation processes such as initiation of cracks and structural phase transformation. Advanced teraflop to petaflop computers make molecular dynamics (MD) simulations of micron-size systems for time-scale of nanoseconds to microseconds possible. With appropriate atomic representation of the material, it can simulate many physical processes on the atomic level. MD simulations have been used to study shock response of Lennard-Jones crystals<sup>26,27</sup> and metals,<sup>28–30</sup> as well as fracture processes in various materials.<sup>31–34</sup> However, little work has been done to simulate fracture in ceramics under ultrahigh strain rate loading.

To gain some insight into the microscopic damage mechanism of alumina under ballistic loading, we carried out MD simulation of  $\alpha$ -alumina substrate impacted on the (0001) surface by a projectile of smaller cross section at 18 km/s. The whole system includes  $540 \times 10^6$  atoms and measures about  $200 \times 200 \text{ nm}^2$  in cross section. Stress, temperature, atomic coordination number, and other physical quantities are computed. Deformation processes, such as slip and twin, and some undocumented deformation patterns are observed. Cracking mechanisms are also studied in the simulation.

This paper is organized into three major sections. First the simulation methodology and system setup are discussed. Subsequently we present results and related discussion in a chronological order of the deformation and fracture events. In the end we summarize the results in the conclusion.

## II. SIMULATION METHODOLOGY

### A. Molecular dynamics

MD is a time integration algorithm that simulates a system of atoms that interact via certain interatomic potential by numerically solving Newton's equations

$$m_i \frac{d^2}{dt^2} \bar{r}_i = \bar{F}_i = -\bar{\nabla}_i V, \quad (1)$$

where  $\bar{r}_i$  is the coordinates of atom  $i$ ,  $\bar{F}_i$  is the total force on the  $i$ th atom, and  $V$  is the interatomic potential.

For a system of  $N$  atoms, there are  $3N$  such second-order differential equations that are solved by time integration. Given the initial positions and momenta of all the atoms, the system's trajectory in the configuration space is integrated over discretized time of interval  $\Delta t$ . At the beginning of each interval, the forces on atoms are calculated using their current positions. Then their positions and momenta are propagated forward in time as  $\bar{r}(t), (d/dt)\bar{r}(t) \Rightarrow \bar{r}(t+\Delta t), (d/dt)\bar{r}(t+\Delta t)$ . The integration method most commonly used is the velocity Verlet algorithm:

$$\begin{aligned} \check{r}(t + \Delta t) &= \check{r}(t) + \frac{d}{dt} \check{r}(t) \Delta t + \frac{1}{2} \frac{d^2}{dt^2} \check{r}(t) \Delta t^2 \\ \frac{d}{dt} \check{r}(t + \Delta t) &= \frac{d}{dt} \check{r}(t) + \frac{1}{2} \left[ \frac{d^2}{dt^2} \check{r}(t) + \frac{d^2}{dt^2} \check{r}(t + \Delta t) \right] \Delta t. \end{aligned} \quad (2)$$

MD can be parallelized computationally to simulate systems of much larger scale than a single computing unit can handle. The total system is spatially decomposed onto certain number of computing units. During any time step, each unit is responsible for computing the forces, updating the velocities and positions of the resident atoms. To include interactions across surfaces, each unit needs information of alien atoms within an external skin of depth  $r_c$ , which is defined to be the range of interatomic interaction. This is done at the beginning of each time step through two-way communications between neighbor units. Subsequently, complete interactions on all resident atoms are calculated, with velocities and positions updated using the velocity Verlet algorithm. At the end of each MD step, the atoms migrating out of the subsystem are removed from the local list and copied over to the corresponding neighbor processes. Physical quantities such as stresses and temperature can be calculated from the atomic positions, velocities, and forces.

### B. Interaction potential

The interaction potential adopted in this MD simulation contains two-body and three-body parts.

The two-body interaction potential between atom pairs  $i$  and  $j$  with  $r=|r_{ij}|$  as the interatomic distance is

$$\varphi_{ij}(r) = \frac{H_{ij}}{r^{n_{ij}}} + \frac{q_i q_j e^{-r/r_{1s}}}{r} - \frac{D_{ij}}{r^4} e^{-r/r_4} - \frac{W_{ij}}{r^6}. \quad (3)$$

The four terms are, from left to right, respectively, steric repulsion, screened Coulomb interaction, charge-dipole interaction, and van der Waals interaction. Here  $H_{ij}$  and  $n_{ij}$  are the strength and exponent of steric repulsion between atoms  $i$  and  $j$ . In the second term,  $q_i$  is the charge of atom  $i$ , and  $r_{1s}$  is the screening length of Coulomb interaction. Similarly,  $D_{ij}$  and  $r_{4s}$  are the strength and screening length of charge-dipole interaction.  $W_{ij}$  is the coefficient of van der Waals interaction.

The three-body interaction potential to describe bond bending and bond stretching for an atom triplet  $j-i-k$  is

$$\varphi_{jik}(r_{ij}, r_{ik}) = \begin{cases} \lambda_{jik} e^{\gamma(r_{ij}-r_0)} e^{\gamma(r_{ik}-r_0)} \frac{(\cos \theta_{jik} - \cos \bar{\theta}_{jik})^2}{1 + c_{jik}(\cos \theta_{jik} - \cos \bar{\theta}_{jik})^2} & \text{for } r_{ij} \leq r_0, r_{ik} \leq r_0 \\ 0 & \text{otherwise,} \end{cases} \quad (4)$$

where  $\lambda_{jik}$  is the strength of the three-body potential,  $\theta_{jik}$  is the angle between vectors  $\mathbf{r}_{ij}$  and  $\mathbf{r}_{ik}$ , and  $\gamma$  and  $c_{jik}$  are constants adjusting the decay of the potential within the three-body interaction range  $r_0$ .

The parameters of the interaction potential are fitted to experimental results of lattice constants, bulk modulus, melting temperature, and cohesive energy. Table I, provided by Vashishta *et al.*,<sup>35</sup> compares the elastic constants from the potential and corresponding experimental values. In the two-body interaction, both the potential and force calculated from its derivative are modified to ensure their continuity at the truncation cutoff  $r_c=0.6$  nm.

$$\begin{aligned} \varphi'_{\alpha\beta}(r) &= \begin{cases} \varphi'_{\alpha\beta}(r) - \varphi'_{\alpha\beta}(r_c) & \text{for } r \leq r_c \\ 0 & r > r_c, \end{cases} \\ \varphi_{\alpha\beta}(r) &= \begin{cases} \varphi_{\alpha\beta}(r) - (r - r_c)\varphi'_{\alpha\beta}(r_c) - \varphi_{\alpha\beta}(r_c) & \text{for } r \leq r_c \\ 0 & r > r_c. \end{cases} \end{aligned} \quad (5)$$

### C. Crystal structure of $\alpha$ -alumina

The  $\alpha$ -alumina structure at 300 K can be constructed using a hexagonal unit cell with  $a=0.4754$  nm and  $c=1.299$  nm.<sup>37</sup> However, in MD simulations, a conventional orthorhombic unit cell is more commonly used. In our potential model the three lattice constants are  $a=0.4754$  nm,  $b=\sqrt{3}a=0.8234$  nm, and  $c=1.299$  nm. Kronberg<sup>38</sup> has described the crystal structure in terms of an approximate hcp anion sublattice (i.e., the basal planes are stacked in an- $ABAB$ -sequence), where the cations take two-thirds of the octahedral interstitial sites in an- $\alpha\beta\gamma$ -order. Combining two sublattices, the stacking sequence of the unit cell would be- $A\alpha B\beta A\gamma B\alpha A\beta B\gamma-$ , giving rise to a large lattice constant  $c$ . In each cation sublattice, the atoms are slightly offset in  $Z$  to form a puckered basal plane. This is due to the electrostatic interaction that draws cation atoms closer to empty octahedral interstitial sites above or below them. The structure is shown in Fig. 1(a). However, for analysis and demonstration purposes, the model is often idealized as stacking of planar anion and cation sheets as in Fig. 1(b).

### D. Simulation setup

The simulated  $\alpha$ -alumina system includes  $540 \times 10^6$  atoms in total and measures  $200 \times 200 \times 130$  nm<sup>3</sup> in size. The entire system is spatially decomposed into 960 subsystems

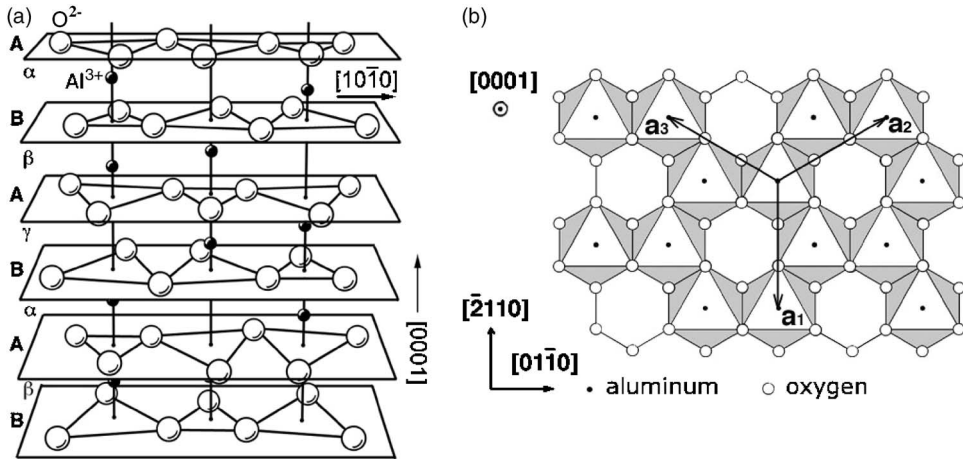
evenly and distributed onto as many processes. The schematic of the simulated system is shown in Fig. 2. The substrate has two free (0001) surfaces at the top and the bottom. It is impacted upon its top free surface by an  $\alpha$ -alumina projectile at  $V_0=18$  km/s. Shaped as a hexagonal cylinder 20 nm wide and 40 nm long, the projectile is subject to a reinforced atomic potential of  $\alpha$ -alumina that measures five times stiffer than normal alumina, with five times the atomic masses. Absorbing boundary condition is applied on all side surfaces of the substrate to eliminate the wave reflection from them, which we will explain in the next paragraph. The trajectory of the system in the configuration space is numerically integrated along the time axis at 1.5 fs intervals. For convenience we define the [0001] direction along the  $Z$  axis, and similarly, [2110] along the  $X$  direction and [0110] along  $Y$  direction, respectively. In order to study the effect of impact speed on deformation patterns, we have also performed simulation at 15 km/s.

Initially, the substrate is a bulk  $\alpha$ -alumina with periodic boundary condition in all three axes. Subsequently, two free (0001) surfaces at the top and bottom are created through two cutting planes. The cutting planes are chosen to be in the middle of the puckered cation sublattices to minimize surface energy.<sup>39</sup> The new surfaces are cooled by constantly quenching the system temperature for 20 000 time steps. After this, the system is subjected to conjugate gradient (CG) to further relax until the energy difference between consecutive

TABLE I. Cohesive energy, bulk modulus, and elastic constants calculated from the interactive potential compared to experimental data. These data along with detailed parameters of the interaction potential, and structural and dynamical properties of crystalline  $\alpha$ -alumina, amorphous, and molten alumina are given by Vashishta *et al.* (Ref. 35)

	MD	Experiments
$E/N$ (eV/atom)	-6.35	-6.35
$B$ (GPa)	253	255
$C_{11}$ (GPa)	523	498
$C_{12}$ (GPa)	147	163
$C_{13}$ (GPa)	129	117
$C_{14}$ (GPa)	7.5	-23
$C_{33}$ (GPa)	427	502
$C_{44}$ (GPa)	135	147
$C_{66}$ (GPa)	174	167 <sup>a</sup>

<sup>a</sup>Calculated from the relation  $C_{66}=(C_{11}-C_{12})/2$ . The experimental data for the elastic constants are from Gieske and Bansch (Ref. 36).



steps reduces to  $10^{-10}$  of the initial energy. After the CG steps, the substrate is relaxed using MD again and thermalizes at a temperature of 10 K over 10 000 time steps. Meanwhile the projectile is cut, prepared through the same thermalization procedures, and positioned on top of the substrate's (0001) surface with a normal velocity of 18 km/s. Absorbing boundary conditions are applied to the velocities of atoms within a range of 10 nm from the side surfaces using a damping function. The damping function scales inversely with an atom's distance from the side surface. This is to eliminate the interference of reflected wave from the side surface. The ensuing impact simulation lasts for 20 000 time steps (or 30 ps) before the substrate totally fractures.

### III. RESULTS AND DISCUSSION

#### A. Penetration of projectile

Upon impact at 18 km/s, the projectile releases its kinetic energy into the target. Meanwhile, the impact surface of the projectile is dramatically heated up due to material resistance and friction. During the early stage of impact, a conic volume in the projectile based on the impact face endures significant impact pressure and its temperature quickly rises above the boiling point.<sup>40</sup> The same process applies to the substrate atoms in front of the impact face. Meanwhile, the projectile material surrounding the cone endures less heating

and melts into a mushroom-shaped crown.<sup>41</sup> As the penetration progresses, the projectile's front surface caves in to form a large low-density concavity in the middle, surrounded by a ring of bulging tip. Subsequently, the already deformed projectile rapidly expands in an almost isotropic pattern driven by the internal pressure. A large amount of projectile atoms also erupts back into the vacuum following the expansion. Around  $t=13$  ps, the projectile reaches the maximum depth of penetration (DOP) of 53 nm when its deformed tip comes to a stop in the impact direction. At the same time, the transverse expansion continues and its center of mass moves backward due to unloading. The DOP as a function of time is shown in Fig. 3.

The impact of the projectile at speeds less than 16 km/s is quite different from the one described above. In this case we observe no vaporization, but only partial to complete liquefaction of the projectile, depending on the impact speed. Also there is no blunting of its tip or subsequent isotropic expansion. The molten tip has its surface atoms peeled off due to friction and trailing on a tail. As a result the projectile

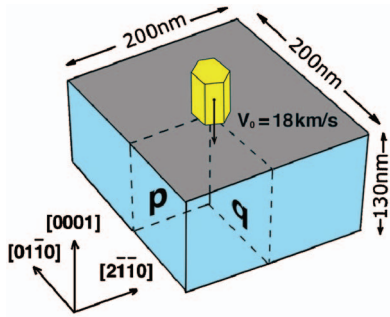


FIG. 2. (Color) The schematics of the simulation setup. A reinforced alumina projectile impacts on an alumina single crystal's (0001) surface at 18 km/s. The simulation embodies  $540 \times 10^6$  atoms in total. The inner planes  $p$  ( $01\bar{1}0$ ) and  $q$  ( $2\bar{1}\bar{1}0$ ) are two major planes where deformations are visualized.

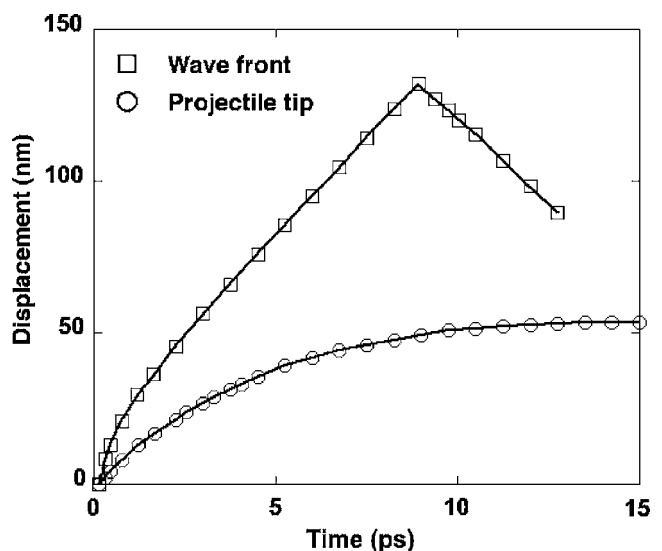


FIG. 3. Shock wave front position in the  $Z$  direction and penetration depth as functions of time. For the wave front position curve, the portion with a negative slope for  $t > 9$  ps corresponds to the rarefaction wave.

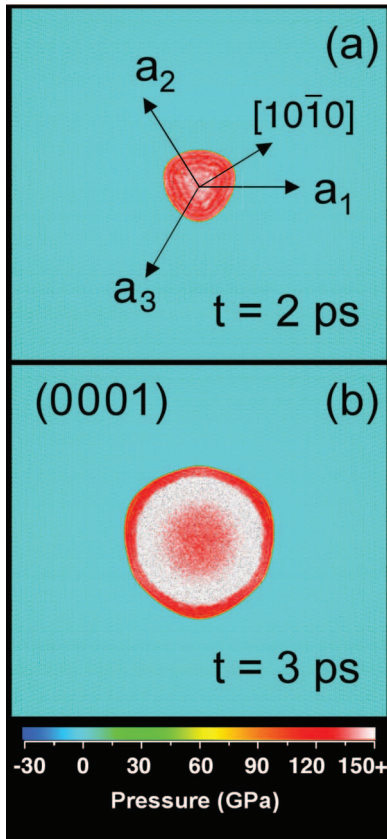


FIG. 4. (Color) The pressure snapshots of the substrate 40 nm under the basal surface where the impact was initiated. From  $t=2$  ps (a) to  $t=3$  ps (b), the symmetry of the shock wave front undergoes a gradual change from threefold to sixfold. This is due to the anisotropies of alumina lattice.

penetrates the target at almost constant speeds, leaving a tunnel behind that is quickly healed by transverse unloading of the substrate.

### B. Shock wave profile

Rapidly compressed by the projectile, the target instantly builds up high local energy density around the impact point. The resulting large gradients in pressure and temperature propagate almost isotropically in the form of a shock wave, whose peak pressure and speed values are 210 GPa and 55 km/s, respectively. As the projectile decelerates and the wave front surface increases during the first 2 ps, the shock wave quickly loses its intensity. It is also decayed by a rarefaction wave off the top free surface, which reduces pressure within the shocked region. As a result, the loading wave's velocity along [0001] drops and stabilizes at the sound speed of 13.2 km/s, after the wave reduces to an elastic one at  $t=2$  ps. A roughly spherical wave front slightly bulging along  $\langle\bar{1}01\rangle$  is observed, which is due to the anisotropy of wave speeds in the lattice. When the wave reaches the side surfaces it is completely absorbed without reflection by the absorbing boundary conditions. The shock front position as a function of time is shown in Fig. 3. At  $t=9$  ps the loading wave hits the substrate's bottom free surface. At the same time, unloading starts at the surface with a rarefaction wave traveling back into the substrate, which is also called unloading wave or tensile wave. Pressure in the region cov-

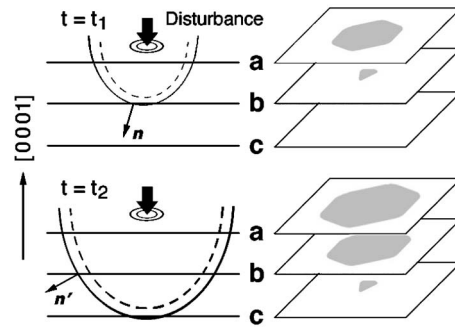


FIG. 5. Schematic of the symmetry transition of wave front's cross section on basal planes. Point source lying in plane  $a$  generates wave (solid curves) that travels at different speeds along crystalline orientations. The cross sections of the wave front on planes  $a-c$  are sketched at  $t=t_1$  and  $t_2$ . Dashed lines denote the wave front in a previous moment.

ered by the rarefaction wave quickly drops into a transient state of roughly  $-20$  GPa. Contrary to the self-steepening effect of the loading wave under positive pressure gradient, the unloading wave front gradually blurs into its surroundings under negative pressure gradient.<sup>42</sup>

To study the anisotropy of wave speed, we divide the substrate into slices parallel to the basal plane. On each slice the wave front is mapped using pressure gradient. At any time, moving up from the wave tip, the wave front's symmetry gradually changes from threefold to sixfold. The same transformation occurs with time in a chosen slice, as shown in Fig. 4.

The phenomenon shown in Fig. 4 is attributed to the alumina structure, which has a stacking sequence of  $A\alpha B\beta A\gamma B\alpha A\beta B\gamma$  along [0001]. The layout of unoccupied cation sites gives the basal layers a threefold inversion symmetry [Fig. 1(a)], and consequently an inverted threefold anisotropy of disturbance in the + and - directions along [0001] is observed. However, in the basal plane, the hexagonal sublattice of both anion and cation [Fig. 1(b)] transmits disturbance with a sixfold in-plane symmetry. Figure 5 illustrates the resulting 3D wave front shape by a point source in plane  $a$ . At  $t=t_1$ , the wave front has a threefold cross section in plane  $b$ . This is because at the intersection point, the direction vector  $n$  of minimal travel time from the point source is almost aligned with the [0001] axis. Along this direction the inverted threefold anisotropy dominates. The same follows for plane  $c$  at  $t=t_2$ . Meanwhile, the wave front always has sixfold symmetry in plane  $a$ , due to the lattice structure in the basal plane. From the threefold cross section in plane  $c$  to the sixfold base in plane  $a$ , it is natural to postulate a transitional surface crossing plane  $b$  at  $t_2$ . So by focusing on plane  $b$ , one will notice a symmetry transition from threefold to sixfold between  $t_1$  and  $t_2$ . Another way to explain the transition is direction vector  $n'$ , along which the disturbance arrives in minimal time from previous wave front, and has a larger component projected on the basal plane compared to  $n$ . Thus it has more sixfold symmetry component at  $t_2$  than at  $t_1$  on plane  $b$ .

For verification, we carry out simulations on bulk  $\alpha$ -alumina of  $(40 \text{ nm})^3$  in size. At the center of the bulk system, we oscillate a small cylindrical volume of the material along the [0001] direction, i.e., along the  $Z$  axis. At  $t$

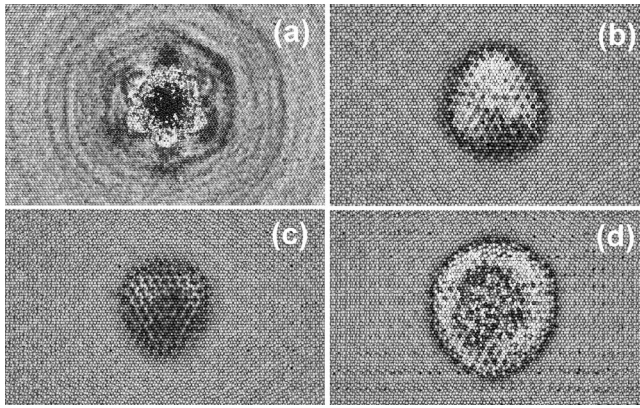


FIG. 6. Simulation on bulk alumina to verify the wave propagation symmetry. A small core in the center produces wave by oscillating in the [0001] direction. All four pictures shown here are pressure profiles on basal planes, where pressure gradients are visualized using grayscale. (a) The pressure snapshot on the basal plane in which the core initially lies at  $t=1$  ps. (b) The pressure snapshot on the basal plane 10 nm above (in the +Z direction) the oscillating core at  $t=1$  ps. (c) The pressure snapshot on the basal plane 10 nm below (in the -Z direction) the oscillating core at  $t=1$  ps. (d) The pressure snapshot on the same plane as in (c) at  $t=2$  ps.

=1 ps, the wave front shape is mapped using pressure on three basal planes at  $Z=Z_{\text{center}}$ ,  $Z=Z_{\text{center}}+10$  nm, and  $Z=Z_{\text{center}}-10$  nm, respectively, in Figs. 6(a)–6(c). At  $Z=Z_{\text{center}}$ , the wave front bears a sixfold symmetry. Meanwhile, on the basal planes above and under the center, the wave front exhibits inverted threefold symmetries. During the next picosecond at  $Z=Z_{\text{center}}-10$  nm, the wave front gradually expands into a sixfold shape as the wave tip travels well past the plane.

### C. Amorphization

First-principles calculation predicts the structural transformation of alumina from corundum to  $\text{Rh}_2\text{O}_3(\text{II})$  phase under a hydrostatic pressure of 78 GPa.<sup>43</sup> For other materials with predicted structural transformation pressure below 100 GPa, such as AlN (Refs. 10 and 44) and SiC,<sup>45,46</sup> impact-loading simulation has revealed a structural transformation wave behind the shock wave front.<sup>47</sup> However, this two-wave structure is not observed in the alumina impact simulation. In shock compression experiments, no phase transformation had been observed under a pressure up to 340 GPa,<sup>16,48,49</sup> until a recent study by Mashimo *et al.*<sup>50</sup> reported a phase transformation to  $\text{Rh}_2\text{O}_3(\text{II})$  structure at a sufficient temperature of 1130 K and pressure of 79 GPa. Although parts of the impacted region in our simulations reach a local temperature of 1500 K and pressure of 100 GPa, the resulting material in these regions appears to be amorphous instead of in  $\text{Rh}_2\text{O}_3$  phase. For validation purpose, hydrostatic compression simulation has been carried out on bulk  $\alpha$ -alumina crystal of the same interaction potential. No phase transformation is observed under a pressure up to 300 GPa at  $T=2000$  K. In addition, the enthalpies of two polymorphs, corundum and  $\text{Rh}_2\text{O}_3(\text{II})$  (structure generated from x-ray experimental data by Lin *et al.*<sup>51</sup>), are almost identical throughout the pressure range. This could imply the absence of transformation mechanism in this interaction potential. To further identify the material's structure close to the

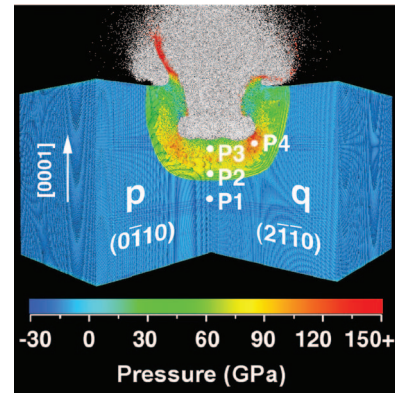


FIG. 7. (Color) Substrate pressure at  $t=4.5$  ps viewed normal to the impact velocity, with its center exposed through a quarter cut. Planes  $p$  and  $q$  correspond to inner surfaces  $p$  and  $q$  in Fig. 2. Four sample cubes P1–P4 of size  $1.2^3 \text{ nm}^3$  are chosen with local density, temperature, and pressure measurements. For each of the four regions, local pair distribution function  $g(r)$  and bond angle distribution are compared to those of the uniform alumina samples prepared with the same densities and temperatures through either slow heating from crystal or fast quenching from molten state.

impact face, we take cubic samples sized  $(1.2 \text{ nm})^3$  at four locations, namely, P1–P4, as shown in Fig. 7. Local densities, pressures, and temperatures at locations P1–P4 are listed in Table II.

Although we anticipate perfect  $\alpha$ -alumina crystal at P1, what structures P2–P4 have remains unclear. From the pressure and temperature values in Table II, P2 and P3 are expected to remain crystalline, as the melting temperature of alumina at 1 bar is around 2800 K given by the interaction potential and is expected to be higher at an elevated pressure. However, pair correlation functions and bond angle distribution analysis reveal that the material at P3 has an amorphized structure, while P2 still exhibits crystalline features. We investigate the state of P4 and P3 by analyzing bulk  $\alpha$ -alumina samples of the same density and temperature prepared using the following procedure. A bulk  $\alpha$ -alumina sample is first hydrostatically compressed to P4's density D4, and then heated up to its temperature T4 through two different paths: Gradual heating to T4 directly (P4'), or gradual heating to 10 000 K and fast quenching to T4 (P4''). Both simulation configurations, P4' and P4'', are compared to P4 configuration using pair correlation functions and bond angle distribution analysis. The same procedure is followed for P3, and results of all the structural analysis are shown in Figs. 8–10.

From Fig. 8, one can conclude that both heating paths lead to a similar structure to that of P4. The mean square displacement measurements in P4' and P4'' suggest that they are in molten states. The differences in the bond angle distribution between P4 and the two reference samples might

TABLE II. The local pressure, temperature, and density values at P1–P4.

	Pressure(GPa)	Temperature(K)	Density	$D/D_{\text{crystal}}$
P4	>150	7300	1.226	
P3	~100	1500	1.172	
P2	~35	45	1.082	
P1	~0	4	1.0	

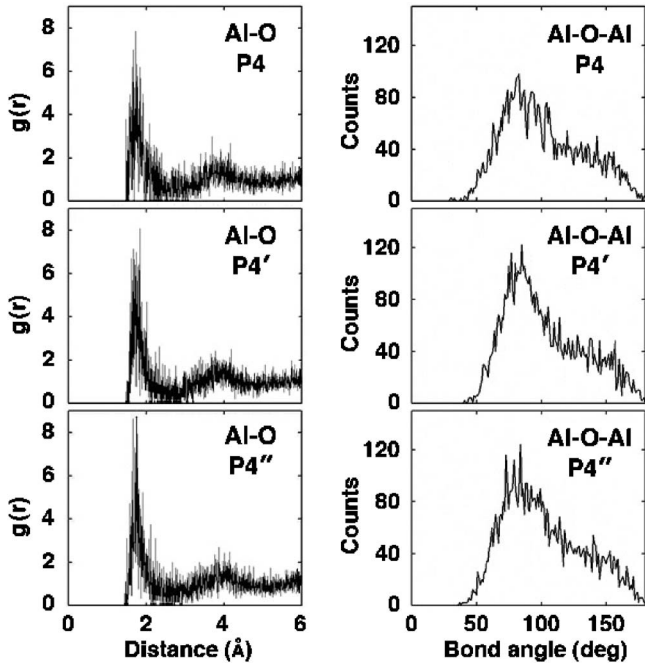


FIG. 8. The pair correlation function  $g(r)$  and bond angle distribution of from top to bottom, respectively, P4, replicated P4 sample through slow heating ( $P4'$ ), and replicated P4 sample through fast quenching ( $P4''$ ). All three samples share common features.

come from the hydrostatic compression used in  $P4'$  and  $P4''$ , whereas in the impact case the region P4 undergoes anisotropic compression. In Fig. 9, only the fast quenching from molten state yields a similar structure ( $P3''$ ) with the impact-loaded sample at P3, while slow heating produces a sample with crystalline characteristics ( $P3'$ ). The mean square displacement measurements in  $P3''$  confirm that it is in an amorphous state.

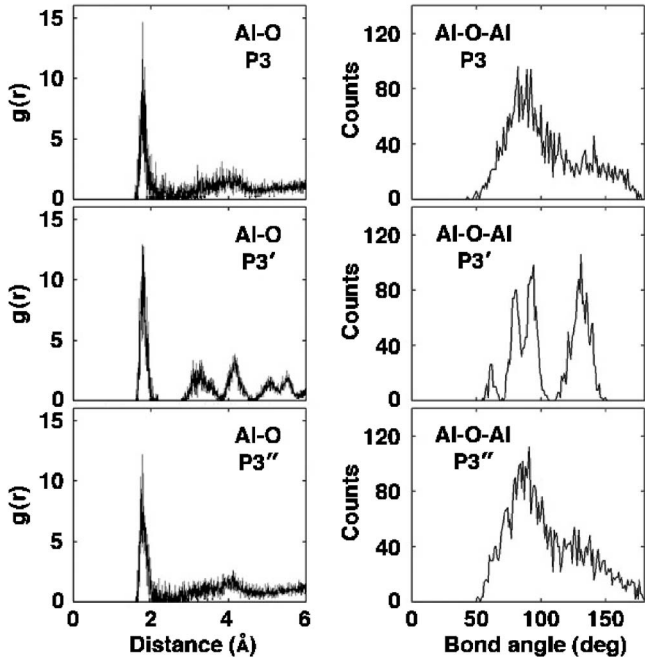


FIG. 9. The pair correlation function  $g(r)$  and bond angle distribution of from top to bottom, respectively, P3, replicated P3 sample through slow heating ( $P3'$ ), and replicated P3 sample through fast quenching ( $P3''$ ). There are similarities between P3 and  $P3''$  but neither resembles  $P3'$ .

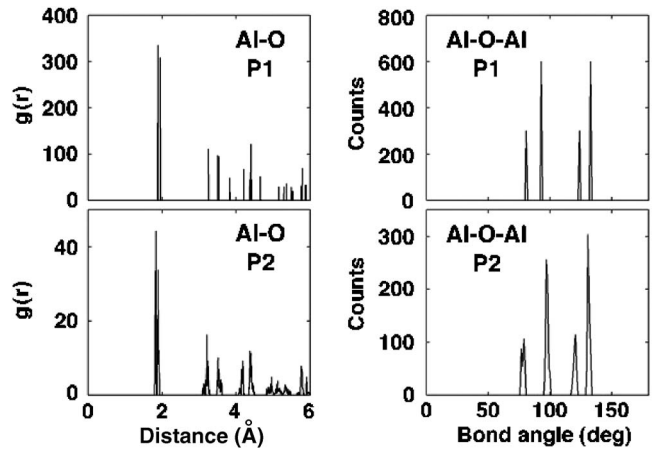


FIG. 10. Plots of pair correlation function  $g(r)$  and bond angle distribution of P1 and P2. The well-isolated peaks imply that they are both in crystalline form.

phous state. The difference between  $P3$  and  $P3'$  implies that temperature alone is insufficient to amorphize the material at  $P3$ . Therefore, the amorphization at  $P3$  is pressure driven by the shock-induced plastic wave. The amorphized region has a similar structure to the amorphous alumina observed by Gutiérrez and Johansson<sup>52</sup> as well as the molten alumina by Ansell *et al.*<sup>53</sup> The pressure-driven amorphization is analogous to the amorphization process observed by Wentzcovitch *et al.* in silica.<sup>54</sup> The crystalline features of P2 in Fig. 10 suggest that its location is behind the elastic wave front but ahead of the trailing plastic wave front. This is consistent with what the shock wave front history suggests. The initial overdrive subsides due to lack of sustained shock loading and pressure concentration.

#### D. Deformation modes

By  $t=5$  ps after the impact, the projectile has lost a large part of its momentum in the [0001] direction and started to expand horizontally. Meanwhile, the stress intensity of the shock has dropped below the elastic limit of alumina.<sup>55,56</sup> Behind the shock wave front, the pressure and temperature are no longer sufficient to drive amorphization, and the material stays crystalline between the shock wave front and the plastic core. The inhomogeneous stresses by anisotropic loading lead to relative sliding between lattice planes. The sliding appears in the form of slips or twins, which stem from the plastic core through dislocations in steady velocities. Viewed from the side, the slips and twins spread out like rays radiating from the core with a roughly constant spacing between the initiation sites. Viewed from the top, they appear to form patterns of either sixfold or threefold symmetry, depending on the orientation of crystalline planes where sliding happens.

The extensive research done on slips and twins in alumina provides abundant references for comparison. A few major systems well studied include basal slip, pyramidal slip, prism slip, basal twin, and rhombohedral twin.<sup>57–61</sup> Many of these deformation modes have been identified in our simulation. The tools to identify deformations include pressure profile, coordination number distribution, and ring analysis. The

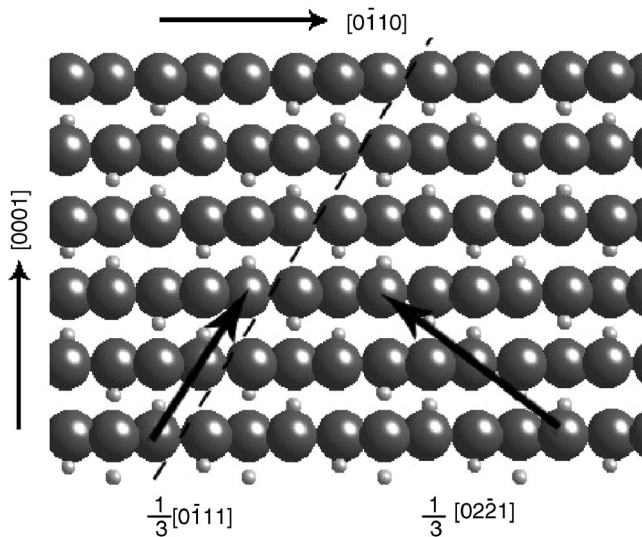


FIG. 11. The prism plane (plane  $q$  in Fig. 2) view of the  $\frac{1}{3}\langle 02\bar{2}1 \rangle$  and  $\frac{1}{3}\langle 0\bar{1}11 \rangle$  Burgers vectors of pyramidal dislocations. Here the large spheres represent oxygen atoms and the small ones are aluminum atoms. The dashed line denotes the  $\{0112\}$  lattice plane that has cation holes only, along which the activation energy of pyramidal dislocation motion is lower.

coordination number of an atom is the number of neighbor atoms with which it is chemically bonded. Ring analysis calculates the numbers of rings of certain length from any atom, where a ring is a shortest close path of chemical bonds. We have designed a ring-analysis algorithm using collision-free spatial hash function to speed up the computation for the  $540 \times 10^6$  atom system.<sup>62</sup> Correlation between these approaches proves effective to identify damages and associate them to known deformation mechanisms. Further discussion follows in the subsections below.

### 1. Pyramidal slips

Pyramidal slips have been observed in the simulation under impact loading along  $[0001]$ . They are initiated and driven by pyramidal dislocations, the only dislocation system in alumina with the  $[0001]$  component in its Burgers vector.<sup>57</sup> Pyramidal dislocations have several possible groups of Burgers vectors, and two of them are along prism planes:<sup>63</sup>  $\frac{1}{3}\langle 10\bar{1}1 \rangle$  and  $\frac{1}{3}\langle 2\bar{0}21 \rangle$ , as shown in Fig. 11. The first group has a lower activation energy because it can happen along  $\{\bar{1}012\}$  crystalline planes of cation holes only,<sup>64</sup> denoted by the dashed line in Fig. 11. In experiments, the second group has never been observed.<sup>57,60</sup>

Starting from 3 ps, when the amorphous region stops growing, pyramidal slips nucleate at the amorphous region boundary. In order to demonstrate the deformation patterns arising from the pyramidal slips, Fig. 12(a) shows the substrate's cross section normal to the impact direction at a depth of 40 nm at 5 ps using deviation from a perfect crystal in coordination number. The white-color region is the deformed projectile. Along  $\{2\bar{1}10\}$  from the center, the projectile invades the substrate further, since these planes are the weak planes under tensile loading<sup>65</sup> (in Fig. 12(a), the white arrow labeled  $[01\bar{1}0]$  points to the intersection of  $(0001)$  and

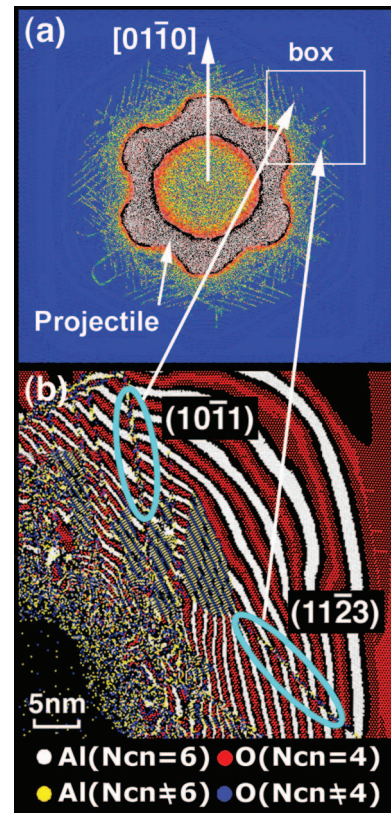


FIG. 12. (Color) Snapshots of pyramidal slips under high shear stress induced by penetration and expansion of the projectile. (a) Basal plane cross section of the whole substrate at depth=40 nm and  $t=5$  ps. Atoms are color coded using coordination numbers. Streaks of pyramidal slips form a hexagramlike pattern. (b) A close-up of the boxed region color coded by atomic species ( $N_{cn}$  means coordination number). Two of the pyramidal slips are circled in cyan and their orientations labeled. Mismatch of atomic layers across these slips arises from the relative sliding between the slip surfaces.

$2\bar{1}10$ ). From the protrusion fronts in the  $\langle 01\bar{1}0 \rangle$  directions, parallel streaks of abnormally coordinated atoms appear along four sets of orientations:  $\{10\bar{1}1\}$ ,  $\{\bar{1}012\}$ ,  $\{2\bar{1}13\}$ , and  $\{4\bar{2}23\}$  [two of them are shown in the cyan ellipses in Fig. 12(b)], which are identified to be pyramidal slips. Visualization of the simulation shows that the slips initiate almost simultaneously and propagate with roughly constant speeds. They are always generated in parallel series to successively relieve the enormous shear caused by the impact. As a result, a shear stress gradient develops from the amorphous core to the surrounding crystalline region. This causes the dislocations closer to the amorphous core to move faster than the outer ones. The maximum speed of dislocation is around 0.7 km/s. The slips eventually form concentric hexagrams in the basal plane before they stop each other at the intersections. All four SPs ( $\{10\bar{1}1\}$ ,  $\{\bar{1}012\}$ ,  $\{2\bar{1}13\}$ , and  $\{4\bar{2}23\}$ ) have been reported in previous experimental and theoretical studies,<sup>66–68</sup> which indicate that  $\{10\bar{1}1\}$  and  $\{2\bar{1}13\}$  pyramidal slips are energetically favorable than  $\{\bar{1}012\}$  and  $\{4\bar{2}23\}$ . However, in the impact simulation, we observe equal amounts of pyramidal slips along all four planes. This is partly because of the isotropic shear stresses caused by the projectile intrusion, while each of the four pyramidal slip families merely has threefold symmetries. Therefore, the en-

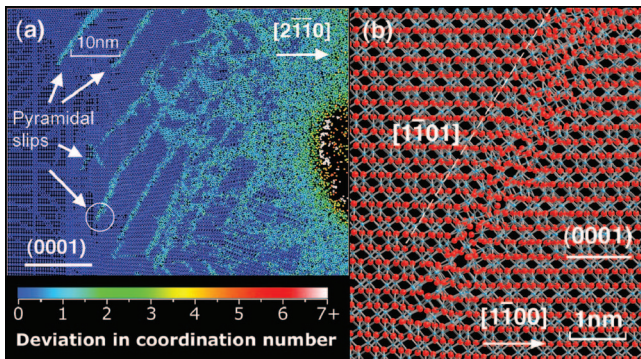


FIG. 13. (Color) (a) Coordination number snapshot of center  $(01\bar{1}0)$  plane (plane  $p$  in Fig. 2) at  $t=8$  ps, where blue atoms have normal coordination number. Pyramidal slips along  $\{2\bar{1}\bar{3}\}$  run parallel with a spacing of 5–8 nm. (b) An up-close view of the circled region in (a) using ball-and-stick representation, rotated to align with the  $(11\bar{2}0)$  prism plane. The circled green stripe in (a) turns out to be a thin stripe of amorphized material along  $(2\bar{1}\bar{3})$ , which intersects the prism plane along  $[1\bar{1}01]$ . These are atoms with abnormal coordinates resulting from the slip.

ergetically favorable slips alone cannot effectively relieve the shear stresses, which geometrically necessitates the presence of the other slips. Also the high temperature and high strain rate associated with hypervelocity impact provide sufficient energy to overcome the high activation barrier of the other slips. For impact simulation at 15 km/s, the pyramidal slips form a similar sixfold pattern initially, which soon becomes threefold as the slips along  $\{10\bar{1}1\}$  and  $\{2\bar{1}\bar{1}3\}$  grow much longer than the other two slip systems. Figure 13(a), a snapshot of the center  $(01\bar{1}0)$  plane (plane  $p$  in Fig. 2) color coded by coordination number, shows that streaks of pyramidal slips along  $\{2\bar{1}\bar{3}\}$  are nearly evenly spaced with 5–10 nm in between. Because of the highly disordered vicinity of these slips, as shown in Fig. 13(b), it is difficult to identify the dislocation processes that accompanied the slip.

## 2. Basal slip and basal twin

Basal slip and basal twin are among the most frequently observed deformation modes in  $\alpha$ -alumina.<sup>20,69</sup> The new model for basal deformation proposed by Bilde-Sørensen *et al.*<sup>70</sup> and Pirouz *et al.*<sup>71</sup> assumes that basal SP slices right through the middle of a puckered cation sublattice with a layer of aluminum on each side. So when basal slip happens, only half of the cations in each cation sublattice move, which allows dislocation motion with no charge transport. It is well accepted that the basal dislocations can be decomposed into two partials as

$$\frac{1}{3}\langle\bar{1}\bar{1}20\rangle \Rightarrow \frac{1}{3}\langle\bar{1}010\rangle + \frac{1}{3}\langle0\bar{1}10\rangle.$$

However, such dislocation process cannot happen on the opposite direction as  $\frac{1}{3}\langle\bar{1}\bar{1}20\rangle$  cannot be decomposed into  $\frac{1}{3}\langle\bar{1}010\rangle$  and  $\frac{1}{3}\langle0\bar{1}10\rangle$ , where the aluminum atoms across the slip plane would come too close and build up high electrostatic energy with such partial dislocations.<sup>57</sup> The unidirectional nature of basal dislocations is illustrated in Fig. 14. The resulting threefold symmetry of basal dislocations is consistent with our observation in the simulation.

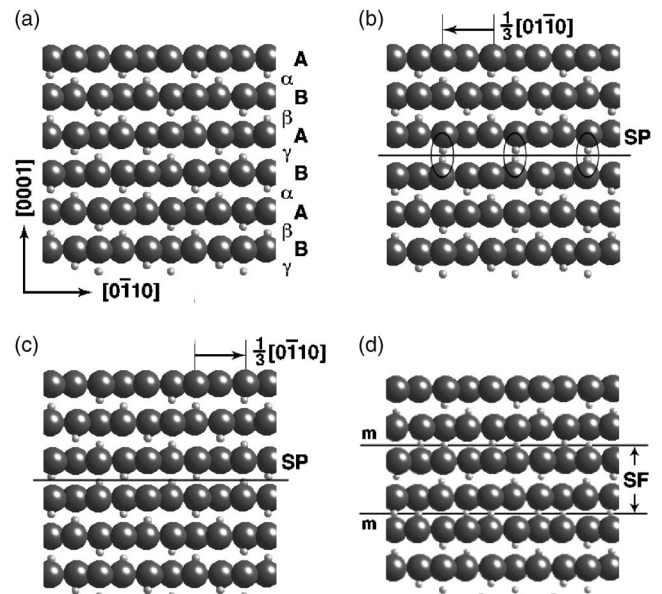


FIG. 14.  $[2\bar{1}\bar{1}0]$  direction view of the corundum lattice's prism plane. (a) The perfect corundum lattice. (b) A case where severe stacking problem happens when the upper half is sheared by  $\frac{1}{3}[01\bar{1}0]$  relative to the bottom, where SP refers to slip plane. (c) The case when the upper half is sheared by  $\frac{1}{3}[0\bar{1}10]$  relative to the bottom and there is no stacking problem caused by the alumina atom pairs. (d) The relaxed crystal structure of (c) which creates a SF and local twinning region between the two  $m$  planes.

After partial slip by  $\frac{1}{3}\langle 0\bar{1}10 \rangle$ , the new charge distribution's symmetry allows two adjacent puckered cation sublattices [labeled  $m$  in Fig. 14(d)] to flatten after relaxation. Therefore  $\frac{1}{3}\langle 0\bar{1}10 \rangle$  partial slips on these adjacent cation layers are forbidden. Between the two flattened layers, a micro-twin forms, which may grow in thickness through repeated  $\frac{1}{3}\langle 0\bar{1}10 \rangle$  partial dislocations on alternating cation layers.<sup>57</sup> This model is consistent with experimental results<sup>72</sup> while some older models<sup>73</sup> are not. The basal twin has the same threefold symmetry with the basal partial dislocation. The energy of stacking fault (SF) caused by the partial dislocation on a basal plane is plotted in Fig. 15.

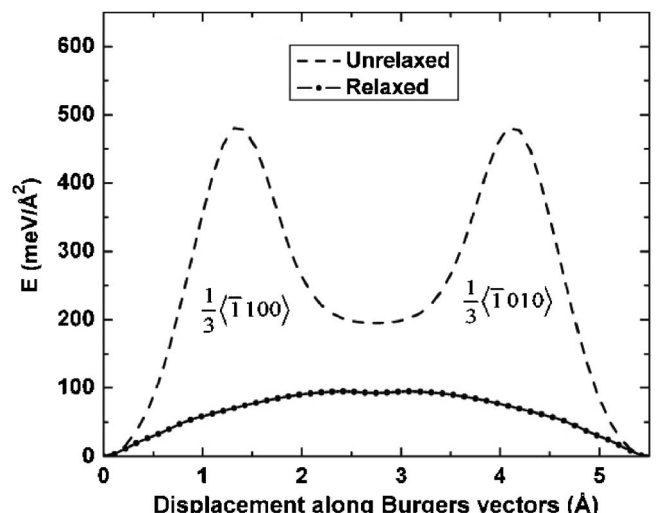


FIG. 15. The generalized SF energy along alumina's basal plane, where results of vertically relaxed system are compared with no relaxation.

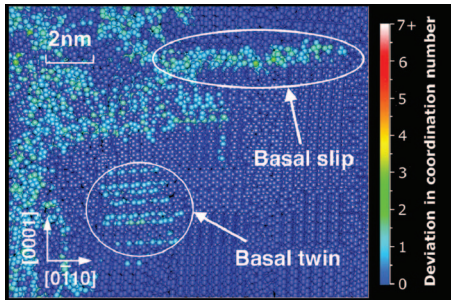


FIG. 16. (Color) The coordination number snapshot on the center prism plane (plane  $q$  in Fig. 2) at  $t=8$  ps. Basal slip is triggered by horizontal expansion of the projectile and bending of basal layers, causing shear along basal planes. Basal twin is also present in this view, appearing on consecutive crystalline layers.

Basal deformations are frequently observed in our simulation due to bending of the basal lattices. A snapshot on the middle ( $\bar{1}\bar{1}0$ ) prism plane (Fig. 16) shows basal deformations including basal slips and basal twins. The critical shear stress for the basal dislocation to advance is 15 GPa, whereas the theoretical value of Peierls stress is 17 GPa.<sup>60</sup> In contrast to the atomistically sharp slip surfaces associated with the basal twins, the basal slip surfaces are often more disordered (see Fig. 16). These deformation patterns are less frequently observed in the 15 km/s simulation.

### 3. Twin along $\{0\bar{1}1\}$

When the projectile's penetration slows down around  $t=6$  ps, a large-deformation region has formed in front of the projectile. The region is roughly a cylindrical frustum with an opening angle of 40 deg. Its top surface is right under the projectile tip, with which it has about the same diameter. The inside of the frustum is directly loaded and builds up a pressure around 40 GPa. The pressure and temperature are insufficient to amorphize the material inside the frustum but the large shear causes various deformations. The deformations that define the frustum surface are twins along  $\{0\bar{1}1\}$  [arrows in Fig. 17(a), basal plane view]. One of them,  $s_1$ , is visualized on a prism plane as well as in Fig. 17(b), and with more details in Fig. 17(c). Shown in Fig. 17(c),  $s_1$  is a twinning region trailing a set of dislocations along  $\{0\bar{1}1\}$ . As the dislocations advance at a roughly constant speed of 8 km/s [see Fig. 17(d)], the twin extends along  $\{0\bar{1}1\}$  with a constant thickness of approximately 1.5 nm. They eventually create steps on the bottom free surface. The twin plane surfaces are rough with disordered atomic arrangements. The resolved shear stress along  $\{0\bar{1}1\}$  around the deformation tip equals to 17 GPa. A few picoseconds later, new twins form outside the previous initiation sites and propagate along  $\{01\bar{2}\}$ . However, they quickly shift to the  $\{0\bar{1}1\}$  orientation through cross slip on basal SPs and leave a large amount of defects behind, which become nucleation sites of microcracks during unloading. The correlation between the number of defects nucleated and twin size is shown in Fig. 17(d). The frustum structure is a unique feature that only emerges under an impact velocity over 15 km/s.

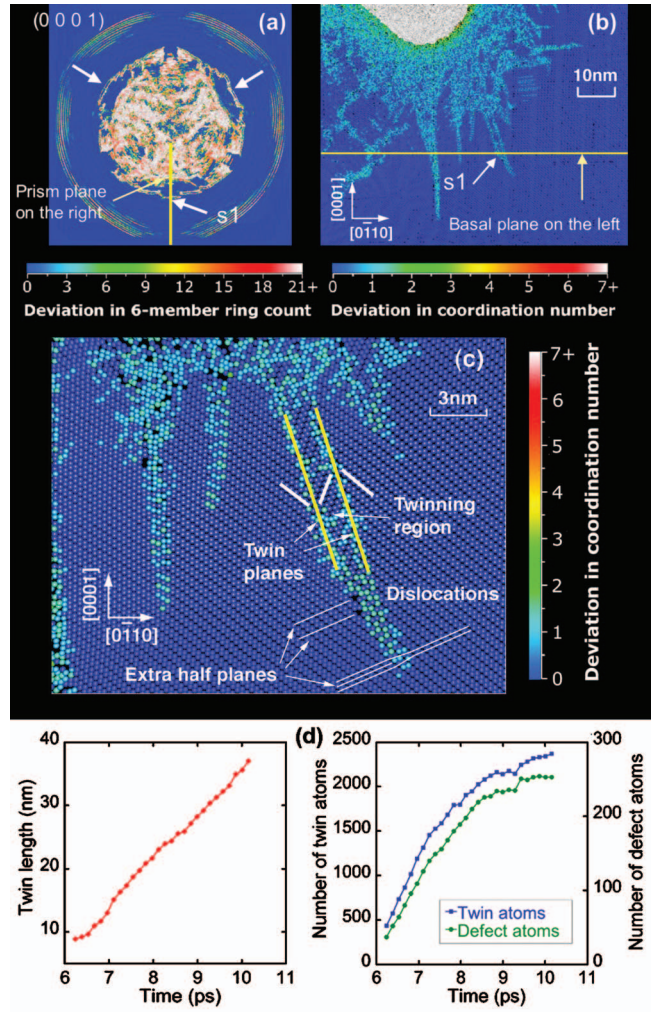


FIG. 17. (Color) (a) Results of the ring analysis in a basal slice 40 nm in front of the projectile tip at  $t=8$  ps. One of the twins along  $\{0\bar{1}1\}$  (white arrows),  $s_1$ , is on the outer boundary of a severely deformed region. It is also shown in (b), the center ( $\bar{1}\bar{1}0$ ) plane (plane  $q$  in Fig. 2) snapshot where atoms are color coded by their coordination numbers. Here the projectile atoms are colored in white. (c) A close-up image of (b) showing details of  $s_1$ , with the twin planes highlighted using yellow lines, and the twin in between is contrasted against normal lattice using thick white line segments. The positions of the dislocations are determined by the misalignment of lattice planes, and extra half planes are singled out with thin white lines. For clarity only aluminum atoms are visualized here. (d) The twin length (left) and the number of defect atoms and twin atoms (right) in a planar twin segment as a function of time. It shows the correlation between twin size and the number of defects.

### 4. Rhombohedral twin

Starting from  $t=6$  ps, pure rhombohedral twins emerge in large amount only inside the frustum surfaced by twins along  $\{011\}$ . The atomic configuration around one twinning deformation is shown in Fig. 18(a). Because there is no slip present, the atoms on the twin surfaces are normal coordinated as in an ideal crystal. Therefore, these twins are distinguishable using the ring analysis but not with the coordination number analysis (see Fig. 19). Viewed normal to either a prism plane or a basal plane, they appear as parallel long streaks along  $\{\bar{1}02\}$ , as shown in Figs. 18(b) and 19(a), respectively. When viewed normal to a prism plane, the twins' width and spacing are multiples of 0.384 nm, where

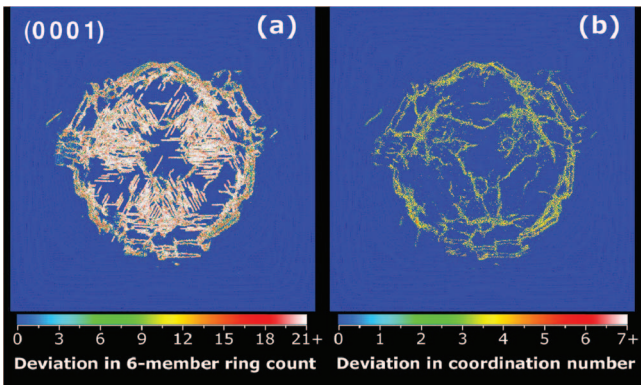


FIG. 18. (Color) (a) Prism plane (plane  $q$  in Fig. 2) view of one rhombohedral twin using ball-and-stick representation. The red spheres are oxygen atoms and blue ones aluminum atoms. Two  $(01\bar{1}2)$  mirror planes are highlighted using yellow lines, and twinned lattice planes using white lines. (b) A thin slice of the prism plane (plane  $q$  in Fig. 2) showing the twinning region. The atoms are color coded by deviation in the number of six-member rings from a perfect crystal, and only deviant atoms are shown. The streaks on the right are twins along  $(01\bar{1}2)$  planes, the same orientation as the one in (a). Those on the left running perpendicular are rhombohedral twins along  $(\bar{1}012)$  and  $(1\bar{1}02)$  planes, which intersect the prism plane along  $[02\bar{2}1]$ . However, their Burgers vector is not along  $[02\bar{2}1]$ .

0.384 equals to the  $\{\bar{1}012\}$  interplanar spacing. As  $\{\bar{1}012\}$  has three possible orientations, twins of different orientations stop each other when they intersect, and generate nanovoids at the intersection. When rarefaction wave from the bottom surface propagates through, the nanovoids grow and coalescence into cracks. Unlike the twins along  $\{0\bar{1}11\}$ , pure rhombohedral twins disappear during unloading, except for the defected regions around their intersections. Rhombohedral twins have been frequently observed in experiments.<sup>74–76</sup>

### E. Structural change

Additional to the slips and twins, structural change is observed in the deformed crystalline region, which appears as large volumes of undercoordinated atoms and clear grain boundaries separating them from normal lattice in Fig. 20. Magnification of those regions reveals a transformation of all aluminum atoms from six coordinated to five coordinated,

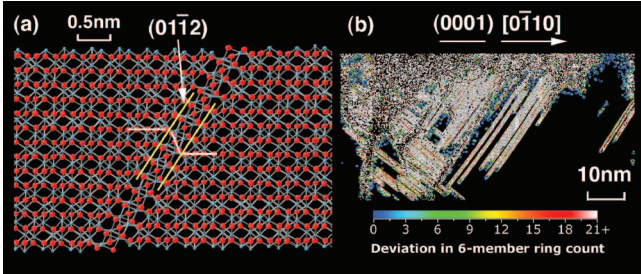


FIG. 19. (Color) Basal snapshots showing symmetry of rhombohedral twin, which are effectively identified using ring analysis. (a) A full-size basal plane cut 80 nm in front of the impact initiation site at  $t=12$  ps. Atoms are color coded by deviation in the number of six-member rings from perfect crystalline atoms (blue) using the gradient bar above. (b) The same plane color coded by deviation in coordination number from perfect crystalline atoms (blue). The three fold structure of rhombohedral twins (parallel streaks of white line segments) in (a) is invisible here.

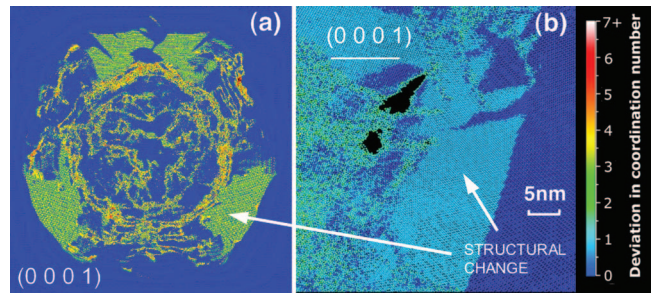


FIG. 20. (Color) Basal plane view of the entire substrate 80 nm in front of the impact point (a) and prism plane (plane  $q$  in Fig. 2) view (b) of some structural change regions by visualizing the deviation in coordination number at  $t=18$  ps when stresses shear the center of the substrate in the  $+Z$  direction due to the unloading. All the aluminum atoms in that region transform from six coordinated to five coordinated. Two-thirds of the oxygen atoms transform from four coordinated to three coordinated.

and two-thirds of the oxygen atoms change from four coordinated to three coordinated. This structural change is attributed to large shear loading normal to the basal plane. As only shear in certain direction triggers the change, shear in the opposite direction causes slip and twin. As shown in Fig. 21, at  $t=6$  ps the shear loading in the prism plane tilts the crystalline layers but causes no structural change. During unloading, the shear direction is reversed. Around  $t=15$  ps the basal lattice planes begin to tilt in the opposite direction. As the shear strain increases, some atomic bonds between aluminum and oxygen atoms snap beyond the stretch limit around  $t=18$  ps. However, after crack nucleation around these structural change regions relieves the shear stresses, the crystalline lattice returns to the original structure. Tests in bulk alumina confirm that the structural change can only be sustained by applying shear stress.

### F. Fracture

When deformations of different orientations intersect, they often form defects at the junctions. For example, intersecting rhombohedral twins (with three possible orientations) generate a disordered crystalline structure with vacancies and nanovoids. Similarly, defects are frequently observed around

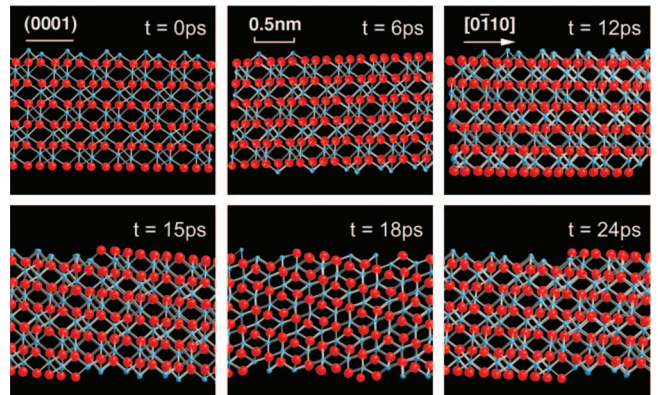


FIG. 21. (Color) Ball-and-stick presentations of atoms around the arrow head in Fig. 20(b) at different time frames, viewed perpendicular to the same prism plane (plane  $q$  in Fig. 2). Here the red spheres represent oxygen atoms and the blue ones aluminum atoms. The structural change appears due to shear in the prism plane ( $t=18$  ps) and fully recovers when the shear stresses are relieved ( $t=24$  ps).

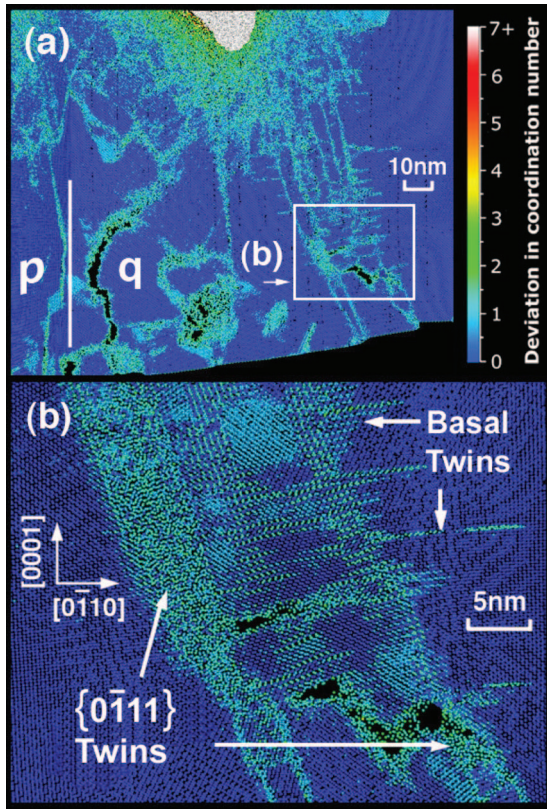


FIG. 22. (Color) (a) Prism plane (plane  $q$  in Fig. 2) view using coordination numbers at  $t=18$  ps, showing the major cracks at the early stage of unloading. The white vertical line on the left denotes the centerline of the substrate with part of plane  $p$  shown on the other side. The long crack next to it initiates from the amorphized stripe where rhombohedral twins intersect. The parallel streaks on the right side are twins along  $\{0\bar{1}11\}$ . (b) A blowup of the boxed region in (a). It demonstrates that cracks initiate around the region where twins along  $\{0\bar{1}12\}$  cross slip to  $\{0\bar{1}11\}$  through basal deformations.

locations that include intersections of slips, intersections of twins, intersections of slip and twin, and grain boundary of structural change grain and amorphous region. In our simulation, the loading wave hits the bottom free surface around  $t=9$  ps and returns as a tensile wave, causing a large amount of microcracks to nucleate around existing nanovoids and subsequently coalesce into major cracks.

After  $t=12$  ps when the unloading wave propagates past where  $\{0\bar{1}12\}$  twins cross slip, some microcracks nucleate from the intersection of two twin systems (basal and  $\{0\bar{1}11\}$ ) and coalesce into bigger cracks [see Fig. 22(a) and its close-up image of Fig. 22(b)]. These cracks zigzag as they toggle between basal planes and  $\{0\bar{1}12\}$  planes. However, their growth is halted around  $t=18$  ps when cracks open up from intersections of rhombohedral twins in the middle of the substrate [see Fig. 22(a), to the left of the boxed region]. These new mode I cracks propagate to the substrate's bottom surface through coalescence with existing nanovoids. They dominate in the early stages of unloading when the middle of the substrate is subjected to the strongest tensile stresses. The crack surfaces are aligned along  $\{2\bar{1}\bar{1}0\}$  (prism) planes. To estimate their fracture toughness, we first locate a microcrack that starts propagating under increasing local tensile stress.

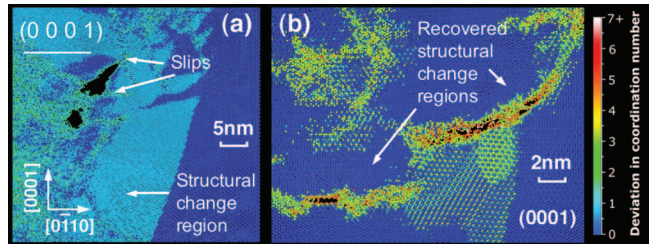


FIG. 23. (Color) (a) Center prism plane (plane  $q$  in Fig. 2) view on the same height with the projectile center at  $t=12$  ps. Fractures are observed on the boundaries between amorphous regions and structural change regions. (b) Basal plane view a few nanometers in front of the cracks in (a). Cracks form on the boundary of structural change regions and normal lattice, which relieves the stress and reverses the structural change.

From the length of the crack and the tensile stress at which it starts propagating, we estimate the fracture toughness to be  $2.0 \pm 0.5$  MPa $\sqrt{\text{m}}$ , which is comparable to an experimentally observed fracture toughness value of  $2.2\text{--}2.5$  MPa $\sqrt{\text{m}}$ .<sup>77,78</sup>

In a few picoseconds, the cracks in the middle heal as cracks in the cross-slip region start to propagate and relieve the tensile stress in the middle. These side cracks follow the  $\{0\bar{1}11\}$  twin planes. Unlike the bottom half where most cracks initiate from intersections of deformations, the top half has different fracture mechanisms as cracks nucleate from the boundaries between normal lattice grain and phase change region or amorphous domain. At  $t=11$  ps, on the same height with the projectile's center, the tensile wave off the top surface initiates cracks from the grain boundary between structural change region and amorphous region, as well as from the boundary between disordered surface of pyramidal slips and structural change region [see Fig. 23(a)]. The initiation of these cracks quickly recovers the structural change region around back to normal lattice [shown in deep blue color around the cracks in Fig. 23(a)]. A few picoseconds later, on the boundary between structural change region and normal lattice a few nanometers below the projectile tip, where some thin disordered structure has formed, cracks form as the unloading waves travel through [see Fig. 23(b)]. Similar to the previous case, the cracking immediately heals the structural change regions around, so they do not coexist with mature cracks in the picture.

At the final stage of the simulation, the cracks in the top and bottom parts of the substrate connect to form the skirt surfaces of two frustums, respectively, whose bases are the top and bottom free surfaces (see Fig. 24). The entire volume bounded by fractures is shaped like an hourglass, with approximate symmetry about the neck plane. The neck is located roughly at the half height of the substrate, which is a few nanometers in front of the projectile tip, with a radius of around 50 nm. For the top frustum, its skirt surface happens to be the boundary of the amorphous core. The bottom frustum's skirt coincides with the connected surfaces of twins. During spallation, the material in the top and bottom frustum volumes ejects with upward and downward velocities, respectively, and the two chunks are projected to eventually detach from sidewalls.

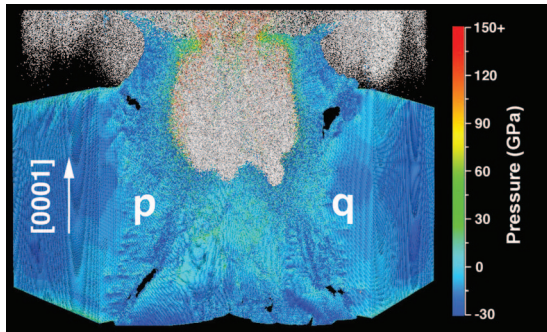


FIG. 24. (Color) The final configuration of the system at  $t=30$  ps, color coded by pressure. The system fractures along the surface of two frustums connected at the neck. In the top half the substrate fractures along the surface of the amorphous region. In the bottom half it fractures along the twin deformations.

### G. Weak planes

In order to identify the weak planes in alumina under tension, we carry out a simulation where bulk alumina atoms on the surface of a cylinder with  $r=20$  nm are continuously pulled outward along radial directions. Beyond a certain strain level in the middle, pores and cracks start to open up in the material. The first major events of cracking happen on  $\{2\bar{1}\bar{1}0\}$  surfaces, as shown in Fig. 25, when the strain exceeds 7%. The tensile stress drops to almost zero from the peak value of 32 GPa as soon as the cracks initiate. This demonstrates that under basal tensile stresses in alumina, the prism planes are the weak planes where cracks tend to propagate along.

### H. Discussion

In the simulation, several modes of deformations are observed. Given a specific time and location, certain deformation modes dominate depending on the loading conditions such as stresses and temperature. In the rapid-loaded region close to the impact face, hydrostatic pressure is more important than shear stresses, which are negligible due to the plastic flow of material. Pressure and temperature together control the amorphization of the substrate. In crystalline regimes outside the amorphous core, shear stresses are more meaningful than hydrostatic pressure. The orientations of slips and twins largely depend on the maximum shear stress direction. Due to alumina's anisotropic structure, its deformation mechanisms are very sensitive to the stress level and orientation. Its unidirectional characteristics along lattice planes lead to asymmetric deformations under isotropic loading. This feature attributes to a wide range of threefold deformation patterns we observe in the simulation, such as rhombohedral twin and structural change. However, the significance of shear stresses does not nullify the role of pressure and temperature in deformation mechanisms. In general, high pressure and high temperature under rapid loading cause deformations with amorphized surfaces, such as in the pyramidal slips we observe. Under comparatively low pressure and low temperature it often leads to perfect deformation surfaces, such as in the rhombohedral twins. These factors in-

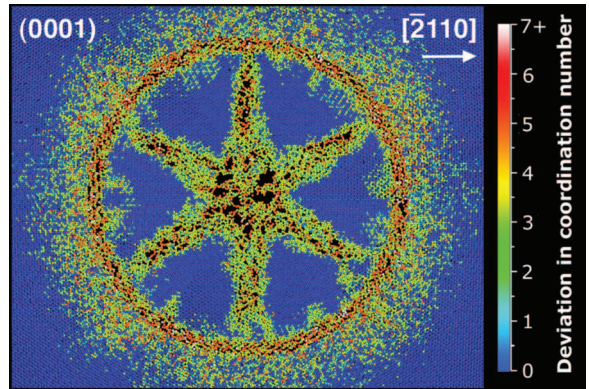


FIG. 25. (Color) Result of cylindrical tensile loading on a bulk alumina sample measuring  $55 \times 50$  nm $^2$  on the basal surface when cracks form in the sample. Atoms are color coded by their coordination number, where colors other than blue refer to the change in coordination numbers. It is clearly demonstrated that the weak planes in the system under basal tensile loading are the prism planes.

terplay and result in distinctive deformation patterns in different stages of the hypervelocity impact simulation.

In summary, we have observed several unique phenomena under a hypervelocity impact of 18 km/s.

- (1) The symmetry of the shock wave front undergoes a threefold to sixfold transition, with pressure-driven amorphization trailing the plastic wave front
- (2) Pyramidal slips nucleate along four sets of crystallographic orientations:  $\{10\bar{1}1\}$ ,  $\{\bar{1}012\}$ ,  $\{2\bar{1}\bar{1}3\}$ , and  $\{4\bar{2}\bar{2}3\}$ . These SPs have different activation energies but occur in nearly equal numbers to form the sixfold deformation pattern.
- (3) Twins along  $\{0\bar{1}11\}$  propagate at a speed of about 8 km/s. The twins help nucleate localized defects, which develop into cracks during tensile unloading.
- (4) The substrate fractures along defected crystalline planes and boundaries of structurally changed regions. From cracks in the system, the fracture toughness along the prism plane is determined to be  $2.0 \pm 0.5$  MPa/m.

### IV. CONCLUSION

The MD simulations of  $\alpha$ -alumina under hypervelocity impact reveal several deformation and fracture mechanisms that are critical to its compressive response. When a reinforced projectile impacts on the substrate at 18 km/s, it induces a shock wave in the substrate. The shock first travels at a velocity above 30 km/s but soon reduces to an elastic wave at 13.2 km/s. The elastic wave front geometry changes as a function of depth due to the anisotropy of alumina crystalline structure. Behind the elastic wave front, an amorphous core forms around the projectile due to the high temperature and pressure generated by the impact loading. Moreover, the local temperature of both the projectile and the substrate around the impact face rises above their boiling/sublimation points. As a consequence the impacted region in the projectile vaporizes and expands in volume. The middle of its impact face collapses into concavity during the expansion, and the only part of its tip that remains condense is a

molten crown surrounding the concavity, which has sixfold bulges along prism planes. After the central collapse of the projectile, the location of maximum pressure in the substrate has shifted off the centerline to ahead of the molten crown. The loading pattern results in a frustum volume of deformations extending all the way to the bottom free surface in the next few picoseconds. Within the frustum we observe abundant instances of rhombohedral twins and their amorphized intersections. Because the twins on the frustum surface effectively relieve the shear stresses, substrate material outside the frustum remains almost perfectly crystalline except for a few pyramidal and basal slips/twins. When the elastic wave front reaches the bottom free surface and returns as a rarefaction wave, it relieves pressure and shear stresses in the substrate. As a consequence some deformation modes disappear and new forms emerge, such as structural change of alumina lattice. During unloading, cracks form under tensile stresses around damages left by intersection of previous deformations. Early cracks close to the centerline heal when spallation opens up larger cracks on the surface of an hourglass-shaped volume. The substrate materials inside the volume are ejected in opposite directions into the free space at the end of the simulation. In the simulation we identify some new deformation processes such as twin along  $\{0\bar{1}11\}$  and structural change under large shear stresses. The critical conditions leading to their occurrences are also investigated. These findings might help understand  $\alpha$ -alumina's behavior under hypervelocity impact.

## ACKNOWLEDGMENTS

This work was partially supported by ARO-MURI's, DoE-BES, DoE-SciDAC, DTRA, and NSF-ITR. Numerical tests were performed at the University of Southern California using the 5400 processor Linux cluster at the Research Computing Facility and the 2048 processor Linux clusters at the Collaboratory for Advanced Computing and Simulations.

- <sup>1</sup>H. Fair, *Int. J. Impact Eng.* **5**, 1 (1987).
- <sup>2</sup>A. Molinari and G. Ravichandran, *J. Appl. Phys.* **95**, 1718 (2004).
- <sup>3</sup>S. Yadav and G. Ravichandran, *Int. J. Impact Eng.* **28**, 557 (2003).
- <sup>4</sup>C. Navarro, M. A. Martinez, R. Cortes, and V. Sanchez-Galvez, *Int. J. Impact Eng.* **13**, 145 (1993).
- <sup>5</sup>I. S. C. Benloulo and V. Sanchez-Galvez, *Int. J. Impact Eng.* **21**, 461 (1998).
- <sup>6</sup>W. P. Schonberg, *Composites, Part A* **31**, 869 (2000).
- <sup>7</sup>E. L. Christiansen, J. L. Crews, J. E. Williamsen, J. H. Robinson, and A. M. Nolen, *Int. J. Impact Eng.* **17**, 217 (1995).
- <sup>8</sup>E. L. Christiansen and J. H. Kerr, *Int. J. Impact Eng.* **20**, 165 (1997).
- <sup>9</sup>M. W. Chen, J. W. McCauley, and K. J. Hemker, *Science* **299**, 1563 (2003).
- <sup>10</sup>M. E. Kipp and D. E. Grady, *J. Phys. IV* **4**, 249 (1994).
- <sup>11</sup>G. Subhash and G. Ravichandran, *J. Mater. Sci.* **33**, 1933 (1998).
- <sup>12</sup>C. J. Shih, M. A. Meyers, V. F. Nesterenko, and S. J. Chen, *Acta Mater.* **48**, 2399 (2000).
- <sup>13</sup>W. H. Gitzen, *Alumina as a Ceramic Material* (The American Ceramic Society, Columbus, OH, 1970).
- <sup>14</sup>B. B. Karki, L. Stixrude, and R. M. Wentzcovitch, *Rev. Geophys.* **39**, 507 (2001).
- <sup>15</sup>Z. Rosenberg, D. Yaziv, Y. Yeshurun, and S. J. Bless, *J. Appl. Phys.* **62**, 1120 (1987).
- <sup>16</sup>T. Mashimo, Y. Hanaoka, and K. Nagayama, *J. Appl. Phys.* **63**, 327 (1988).
- <sup>17</sup>D. E. Grady, *Mech. Mater.* **29**, 181 (1998).
- <sup>18</sup>L. C. Chhabildas, L. N. Kmetyk, W. D. Reinhart, and C. A. Hall, *Int. J. Impact Eng.* **17**, 183 (1995).
- <sup>19</sup>J. Lankford, W. W. Predebon, J. M. Staehler, G. Subhash, B. J. Pletka, and C. E. Anderson, *Mech. Mater.* **29**, 205 (1998).
- <sup>20</sup>H. M. Chan and B. R. Lawn, *J. Am. Ceram. Soc.* **71**, 29 (1988).
- <sup>21</sup>J. M. Staehler, W. W. Predebon, B. J. Pletka, and G. Subhash, *Mater. Sci. Eng., A* **291**, 37 (2000).
- <sup>22</sup>D. Sherman and I. Be'ery, *J. Mater. Sci.* **35**, 1283 (2000).
- <sup>23</sup>J. M. Staehler, W. W. Predebon, B. J. Pletka, and G. Subhash, *JOM* **47**, 60 (1995).
- <sup>24</sup>C. J. Hayhurst, H. J. Ranson, D. J. Gardner, and N. K. Birnbaum, *Int. J. Impact Eng.* **17**, 375 (1995).
- <sup>25</sup>C. H. M. Simha, S. J. Bless, and A. Bedford, *Int. J. Impact Eng.* **27**, 65 (2002).
- <sup>26</sup>B. L. Holian and P. S. Lomdahl, *Science* **280**, 2085 (1998).
- <sup>27</sup>V. V. Zhakhovskii, S. V. Zybin, K. Nishihara, and S. I. Anisimov, *Phys. Rev. Lett.* **83**, 1175 (1999).
- <sup>28</sup>E. M. Bringa, J. U. Cazamias, P. Erhart, J. Stolken, N. Tanushev, B. D. Wirth, R. E. Rudd, and M. J. Caturla, *J. Appl. Phys.* **96**, 3793 (2004).
- <sup>29</sup>K. Kadau, T. C. Germann, P. S. Lomdahl, and B. L. Holian, *Science* **296**, 1681 (2002).
- <sup>30</sup>E. M. Bringa, A. Caro, Y. M. Wang, M. Victoria, J. M. McNaney, B. A. Remington, R. F. Smith, B. R. Torralva, and H. Van Swygenhoven, *Science* **309**, 1838 (2005).
- <sup>31</sup>F. F. Abraham, J. Q. Broughton, N. Bernstein, and E. Kaxiras, *Europhys. Lett.* **44**, 783 (1998).
- <sup>32</sup>K. S. Cheung and S. Yip, *Phys. Rev. Lett.* **65**, 2804 (1990).
- <sup>33</sup>S. J. Zhou, P. S. Lomdahl, A. F. Voter, and B. L. Holian, *Eng. Fract. Mech.* **61**, 173 (1998).
- <sup>34</sup>M. Ross and L. H. Yang, *Phys. Rev. B* **64**, 134210 (2001).
- <sup>35</sup>P. Vashishta, R. K. Kalia, A. Nakano, and J. P. Rino, *J. Appl. Phys.* **101**, 103515 (2007).
- <sup>36</sup>J. H. Gieske and G. R. Barsch, *Phys. Status Solidi* **29**, 121 (1968).
- <sup>37</sup>N. Ishizawa, T. Miyata, I. Minato, F. Marumo, and S. Iwai, *Acta Crystallogr., Sect. B: Struct. Crystallogr. Cryst. Chem.* **36**, 228 (1980).
- <sup>38</sup>M. L. Kronberg, *Acta Metall.* **5**, 507 (1957).
- <sup>39</sup>M. Baudin and K. Hermansson, *Surf. Sci.* **474**, 107 (2001).
- <sup>40</sup>D. A. Shockley, D. R. Curran, J. E. Osher, and H. H. Chau, *Int. J. Impact Eng.* **5**, 585 (1987).
- <sup>41</sup>C. E. Anderson, D. L. Littlefield, and J. D. Walker, *Int. J. Impact Eng.* **14**, 1 (1993).
- <sup>42</sup>J. R. Asay and M. Shahinpoor, *High Pressure Shock Compression of Solids* (Springer-Verlag, New York, 1993).
- <sup>43</sup>W. H. Duan, R. M. Wentzcovitch, and K. T. Thomson, *Phys. Rev. B* **57**, 10363 (1998).
- <sup>44</sup>M. Ueno, A. Onodera, O. Shimomura, and K. Takemura, *Phys. Rev. B* **45**, 10123 (1992).
- <sup>45</sup>T. Sekine and T. Kobayashi, *Phys. Rev. B* **55**, 8034 (1997).
- <sup>46</sup>F. Shimojo, I. Ebbsjo, R. K. Kalia, A. Nakano, J. P. Rino, and P. Vashishta, *Phys. Rev. Lett.* **84**, 3338 (2000).
- <sup>47</sup>P. S. Branicio, R. K. Kalia, A. Nakano, and P. Vashishta, *Phys. Rev. Lett.* **96**, 1 (2006).
- <sup>48</sup>R. A. Graham and W. P. Brooks, *J. Phys. Chem. Solids* **32**, 2311 (1971).
- <sup>49</sup>D. Erskine, International Conference of the International Association for Research and Advancement of High Pressure Science and Technology, Colorado Springs, CO, 1993 (unpublished).
- <sup>50</sup>T. Mashimo, K. Tsumoto, K. Nakamura, Y. Noguchi, K. Fukuoka, and Y. Syono, *Geophys. Res. Lett.* **27**, 2021 (2000).
- <sup>51</sup>J. F. Lin, O. Degtyareva, C. T. Prewitt, P. Dera, N. Sata, E. Gregoryanz, H. K. Mao, and R. J. Hemley, *Nat. Mater.* **3**, 389 (2004).
- <sup>52</sup>G. Gutierrez and B. Johansson, *Phys. Rev. B* **65**, 104202 (2002).
- <sup>53</sup>S. Ansell, S. Krishnan, J. K. R. Weber, J. J. Felten, P. C. Nordine, M. A. Beno, D. L. Price, and M. L. Saboungi, *Phys. Rev. Lett.* **78**, 464 (1997).
- <sup>54</sup>R. M. Wentzcovitch, C. da Silva, J. R. Chelikowsky, and N. Binggeli, *Phys. Rev. Lett.* **80**, 2149 (1998).
- <sup>55</sup>T. J. Ahrens, W. H. Gust, and E. B. Royce, *J. Appl. Phys.* **39**, 4610 (1968).
- <sup>56</sup>N. K. Bourne, *Proc. R. Soc. London, Ser. A* **457**, 2189 (2001).
- <sup>57</sup>A. H. Heuer, K. P. D. Lagerlöf, and J. Castaing, *Philos. Mag. A* **78**, 747 (1998).
- <sup>58</sup>J. Castaing, A. He, K. P. D. Lagerlöf, and A. H. Heuer, *Philos. Mag. A* **84**, 1113 (2004).
- <sup>59</sup>S. J. Chen and D. G. Howitt, *Philos. Mag. A* **78**, 765 (1998).
- <sup>60</sup>K. P. D. Lagerlöf, A. H. Heuer, J. Castaing, J. P. Riviere, and T. E. Mitchell, *J. Am. Ceram. Soc.* **77**, 385 (1994).

- <sup>61</sup>W. D. Scott and K. K. Orr, *J. Am. Ceram. Soc.* **66**, 27 (1983).
- <sup>62</sup>C. Zhang, B. Bansal, P. S. Branicio, R. K. Kalia, A. Nakano, A. Sharma, and P. Vashishta, *Comput. Phys. Commun.* **175**, 339 (2006).
- <sup>63</sup>J. D. Snow and A. H. Heuer, *J. Am. Ceram. Soc.* **56**, 153 (1973).
- <sup>64</sup>C. T. Bodur, J. Chang, and A. S. Argon, *J. Eur. Ceram. Soc.* **25**, 1431 (2005).
- <sup>65</sup>The sixfold symmetry formed by the weak planes is not a direct consequence of the projectile's geometry, because it initially has six corners aligned along the  $(2\bar{1}\bar{1}0)$ .
- <sup>66</sup>R. E. Tressler and D. J. Barber, *J. Am. Ceram. Soc.* **57**, 13 (1974).
- <sup>67</sup>J. Cadoz and B. Pellissier, *Scr. Metall.* **10**, 597 (1976).
- <sup>68</sup>D. M. Kotchick, B. J. Busovne, R. E. Tressler, and D. J. Barber, *J. Mater. Sci.* **17**, 1977 (1982).
- <sup>69</sup>J. Castaing, A. Munoz, D. G. Garcia, and A. D. Rodriguez, *Mater. Sci. Eng., A* **233**, 121 (1997).
- <sup>70</sup>J. B. Bilde-Sørensen, B. F. Lawlor, T. Geipel, P. Pirouz, A. H. Heuer, and K. P. D. Lagerlöf, *Acta Mater.* **44**, 2145 (1996).
- <sup>71</sup>P. Pirouz, B. F. Lawlor, T. Geipel, J. B. Bilde-Sørensen, A. H. Heuer, and K. P. D. Lagerlöf, *Acta Mater.* **44**, 2153 (1996).
- <sup>72</sup>T. Geipel, J. B. Bilde-Sørensen, B. F. Lawlor, P. Pirouz, K. P. D. Lagerlöf, and A. H. Heuer, *Acta Mater.* **44**, 2165 (1996).
- <sup>73</sup>S. J. Chen and D. G. Howitt, *Acta Metall. Mater.* **40**, 3249 (1992).
- <sup>74</sup>A. H. Heuer, *Philos. Mag.* **13**, 379 (1966).
- <sup>75</sup>T. Geipel, K. P. D. Lagerlöf, P. Pirouz, and A. H. Heuer, *Acta Metall. Mater.* **42**, 1367 (1994).
- <sup>76</sup>B. J. Inkson, *Acta Mater.* **48**, 1883 (2000).
- <sup>77</sup>P. F. Becher, *J. Am. Ceram. Soc.* **59**, 59 (1976).
- <sup>78</sup>M. Iwasa and R. C. Bradt, *Am. Ceram. Soc. Bull.* **60**, 374 (1981).